Electronic Structure

OPEN ACCESS

TECHNICAL NOTE

Electronic structure of cesium-based photocathode materials from density functional theory: performance of PBE, SCAN, and HSE06 functionals

Holger-Dietrich Saÿnick[1] and **Caterina Cocchi**[1,2,*]

[1] Carl von Ossietzky Universität Oldenburg, Physics Department, D-26129 Oldenburg, Germany
[2] Humboldt-Universität zu Berlin, Physics Department and IRIS Adlershof, D-12489 Berlin, Germany
[*] Author to whom any correspondence should be addressed.

E-mail: caterina.cocchi@uni-oldenburg.de

Keywords: multi-alkali antimonides, density-functional theory, exchange–correlation functional

RECEIVED
14 December 2020

REVISED
29 March 2021

ACCEPTED FOR PUBLICATION
23 April 2021

PUBLISHED
21 May 2021

Abstract

The development of novel materials for vacuum electron sources in particle accelerators is an active field of research that can greatly benefit from the results of *ab initio* calculations for the characterization of the electronic structure of target systems. As state-of-the-art many-body perturbation theory calculations are too expensive for large-scale material screening, density functional theory offers the best compromise between accuracy and computational feasibility. The quality of the obtained results, however, crucially depends on the choice of the exchange–correlation potential, v_{xc}. To address this essential point, we systematically analyze the performance of three popular approximations of v_{xc} [PBE, strongly constrained and appropriately normed (SCAN), and HSE06] on the structural and electronic properties of bulk Cs_3Sb and Cs_2Te as representative materials of Cs-based semiconductors employed in photocathode applications. Among the adopted approximations, PBE shows expectedly the largest discrepancies from the target: the unit cell volume is overestimated compared to the experimental value, while the band gap is severely underestimated. On the other hand, both SCAN and HSE06 perform remarkably well in reproducing both structural and electronic properties. Spin–orbit coupling, which mainly impacts the valence region of both materials inducing a band splitting and, consequently, a band-gap reduction of the order of 0.2 eV, is equally captured by all functionals. Our results indicate SCAN as the best trade-off between accuracy and computational costs, outperforming the considerably more expensive HSE06.

1. Introduction

Computational methods for material modeling have finally reached into almost all the areas of materials science and discovery, including those fields that, for historical reasons and scientific distance, are far away from condensed-matter physics. Among them, the design and production of photocathode materials for particle accelerators is certainly worth a mention [1, 2]. The most recent advances in this field have imposed a paradigm shift driven by the necessity to develop vacuum electron sources producing increasingly focused particle beams with minimized mean transverse emittance [3–5]. These characteristics can be best achieved through the development of photocathodes based on semiconducting materials which absorb visible light close to the infrared threshold. Alkali antimonides and tellurides generally fulfill this requirement and have been extensively investigated in this context [3, 6–8] along with conventional semiconductors like GaAs [8–10] and popular thermoelectric materials such as PbTe [11, 12].

The search for novel semiconducting materials with optimized characteristics for photocathode applications greatly benefits from *ab initio* quantum-mechanical simulations. Reliable predictions of material compositions and of the corresponding electronic properties are seen as a complement and, in some cases, even as

a replacement of the expensive trial-and-error experimental growth and characterization procedures [13–18]. To this end, multi-purpose databases of materials properties computed from density functional theory (DFT), such as NOMAD [19], Materials Project [20], the Open Quantum Materials Database [21], or Materials Cloud [22], are regarded with particular interest for a quick screening of suitable compounds and also as a source of input data for photoemission models [23]. Yet, the vast majority of the electronic-structure information stored in these databases are obtained under semi-local approximations of the exchange–correlation potential (v_{xc}). As such, these data are likely suitable only for a *qualitative* assessment of properties that are relevant for photoemission.

Recent studies on Cs-based multi-alkali antimonide crystals based on many-body perturbation theory (MBPT) provide state-of-the-art references for the electronic and optical characteristics of these materials [24, 25]. However, these methods are too expensive to be used for high-throughput screening, or in the simulations of surfaces and defected systems, which more closely reflect the intrinsic features of the real materials at significantly large computational costs and complexity. A good compromise is given by advanced approximations of v_{xc}, which have undergone impressive progress in the last decade [26, 27]. Recent developments include new parametrizations in the class of meta-generalized gradient approximation (GGA) functionals [28–31], approximations based on machine-learning methods [32, 33], and improved descriptions of the long-range dispersion interaction [34–37]. Range-separated hybrid functionals and meta-GGA approximations are presently efficiently implemented in many DFT packages [38–40] and, as such, can be routinely used in the *ab initio* simulations of large systems.

To reliably take advantage of DFT calculations in the study of Cs-based photocathode materials, a systematic comparison between the performance of against reliable references is urgently needed. Similar studies were performed either on specific families of materials such as lead chalcogenides (see, e.g. reference [41]), or on new functionals [42–44]. General benchmark studies on solids [45–47] are also a valuable starting point for reference, but the multi-atomic composition of photocathode materials as well as their peculiar chemical properties demand dedicated analysis. This is precisely the scope of this work.

Herein, we investigate the structural and electronic properties of cesium antimonide (Cs_3Sb) and cesium telluride (Cs_2Te), two semiconductors largely employed in the context of photocathode research, in the framework of DFT with different approximations of v_{xc}. Having the practical application in mind, we settled to consider functionals that are implemented and 'ready to use' in a large number of DFT programs, but also represent different levels of exchange–correlation approximations. To this end, we choose three well-established functionals representative for increasing levels of sophistication in the treatment of the exchange–correlation potential, namely, the semi-local Perdew–Burke–Ernzerhof functional [48] implementing the GGA, the strongly constrained and appropriately normed (SCAN) parameterization of the meta-GGA [49], and the Heyd–Scuseria–Ernzerhof range-separated hybrid functional HSE06 [50]. These functionals are prominent representatives of their respective class of approximations (GGA, meta-GGA, and hybrids) that are widely applied to solids. Among the three considered approximations for v_{xc}, meta-GGA is certainly the least mature one, as testified by the number of new developments [28, 51–53] and recent benchmark studies [42–44, 54] dedicated to it. In this developing scenario, the choice of considering SCAN is partly driven by our own positive experience with this functional.

After the optimization of the lattice parameters, which we benchmark against experimental values, we compute band structure and density of states (DOS) of the target systems. The resulting band-gap is contrasted with GW_0 results from MBPT. Our results show that the SCAN functional is an excellent choice in terms of accuracy and computational efficiency and an overall improvement to the PBE functional. We finally assess the performance of the three aforementioned functionals in describing spin–orbit coupling (SOC) effects, which are known to be relevant in the investigated materials, as they are composed of relatively heavy atomic species. We find that SOC, which has a relatively small effect on the electronic properties of both materials, is equally captured by all considered v_{xc} approximations.

This paper is organized as follows. In section 2 the theoretical background of our calculations is reviewed and the relevant computational details are summarized. The body of results is presented in section 3, including the analysis of structural and electronic properties as well as SOC. Summary and conclusions are reported in section 4.

2. Theoretical background and computational details

The results of this work are obtained using DFT [56] within the Kohn–Sham (KS) scheme, which maps the many-body system into an auxiliary system of non-interacting electrons with the same density as the fully interacting one [57]. In this framework, one has to solve for each (valence) electron *i* the KS equations, which

in atomic units read:

$$\left[-\frac{1}{2}\nabla^2 + v_\mathrm{s}\left(\mathbf{r}\right)\right]\varphi_i\left(\mathbf{r}\right) = \epsilon_i^{\mathrm{KS}}\varphi_i\left(\mathbf{r}\right). \tag{1}$$

The eigenvalue ϵ_i^{KS} is the KS energy per particle and the eigenfunction $\varphi_i\left(\mathbf{r}\right)$ the KS wave function. The Hamiltonian operator in square brackets contains two terms, namely the kinetic energy operator and the effective potential per particle

$$v_\mathrm{s}(\mathbf{r}) = v_\mathrm{ext}(\mathbf{r}) + v_\mathrm{H}(\mathbf{r}) + v_\mathrm{xc}(\mathbf{r}), \tag{2}$$

including the external potential v_ext, accounting for the electron–nuclear interaction in absence of external fields, the Hartree potential, v_H, and, the exchange–correlation potential v_xc, the exact form of which is unknown.

The simplest approximation of v_xc, proposed already by Kohn and Sham in their seminal paper [57], consists of treating exchange and correlation effects as in the homogeneous electron gas. On the next rung, we find the GGA, in which v_xc is derived from the local electron density and its gradient. The PBE parameterization of GGA is adopted in this work. Taking one step further consists of approximating v_xc including also the kinetic energy density: this is the so-called meta-GGA approximation. As a representative of this level of approximation, which is currently explored in a number of development and benchmark studies [28, 42–44, 51–54], we employ herein the SCAN functional [49], which fulfills all the constraints for semi-local exchange–correlation functionals and has shown superiority in comparison to many other local and semi-local approximations on a broad range of systems [58, 59]. Very recently, two regularized versions of the SCAN functional have been proposed, namely rSCAN [30] and r^{2}SCAN [31]. The performance of the former is reported in the appendix.

In parallel, another class of approximations for v_xc has been developed in the last two decades, the so-called *hybrid functionals* incorporating a fixed amount of Hartree–Fock exchange correcting the underlying semi-local DFT approximation [60]. Thanks to the presence of a fraction of Hartree–Fock exchange, the self-interaction error, which affects also meta-GGA functionals [58], is alleviated. More recently, this recipe has been further improved through the introduction of *range-separated hybrid functionals*, in which the treatment of the exchange-interaction additionally depends on the range between the orbitals. Here, as a representative of this class, we use the HSE06 functional [50] which has shown remarkable success in the description of bulk properties for semiconducting and insulating condensed systems [61]. In this functional, the electron–electron interaction is split into a short-range and a long-range part: the short range part of the functional consists of 75% of the semi-local PBE xc functional and 25% of non-local Hartree–Fock exchange; in the long range part the functional coincides with PBE.

Other relevant aspects in the solution of the KS equation concern the treatment of core electrons and the choice of the basis set. In this work, we choose the all-electron full-potential implementation of FHI-aims [62]. This package uses numerical atom-centered orbitals as basis set for all electrons. The zero-order regular approximation is applied to correct for relativistic effects of the core-electrons. Additionally, a non-self-consistent post-scf approximation is applied to account for SOC [63]. These calculations are carried out with *intermediate* settings for basis-set and integration grids. A 18 ×18× 18 and a 6 ×12× 6 **k**-grid is chosen for Cs_3Sb and Cs_2Te, respectively. In both cases the convergence of the **k**-grid is checked for the PBE functional. The unit cells of both materials are optimized separately for each functional by calculating the stress tensor until the forces acting on each atom are converged below 1.0×10^{-3} eV Å^{-1}.

In absence of reliable experimental references for Cs_2Te and Cs_3Sb single crystals, we benchmark the accuracy of the DFT band gaps against the outcomes of *GW* calculations [64] in the partially self-consistent flavor GW_0 [65, 66]. In this formalism, the screened Coulomb potential W_0 is evaluated in a single-shot procedure, while the single-particle Green's function G is updated self-consistently. These calculations are performed with the all-electron full-potential code `exciting`, which implements the linearized augmented plane wave plus local orbital method [67, 68]. The size of the basis set is determined by the radius of the muffin-tin (MT) spheres around the nuclei and the plane wave cutoff. The local orbitals available in the default species files are included in the calculations. We anticipate that this can lead to a systematic underestimation of the band gaps [68]. An MT radius of 1.8 and 2.5 bohr is used for both species in Cs_2Te and Cs_3Sb, respectively. A plane-wave cutoff of 8.0 Ha is adopted in both cases. GW_0 calculations are performed on top of the PBE electronic structure obtained upon sampling the Brillouin zone with an 8 ×8× 8 **k**-mesh in Cs_3Sb and 4 ×8× 4 in Cs_2Te. In the GW_0 step, a 6 ×6× 6 **k**-grid is used for Cs_3Sb and a 3 ×6× 3 one in Cs_2Te. Screening is computed in the random-phase approximation including 200 empty states in both systems. It is worth noting that, while the

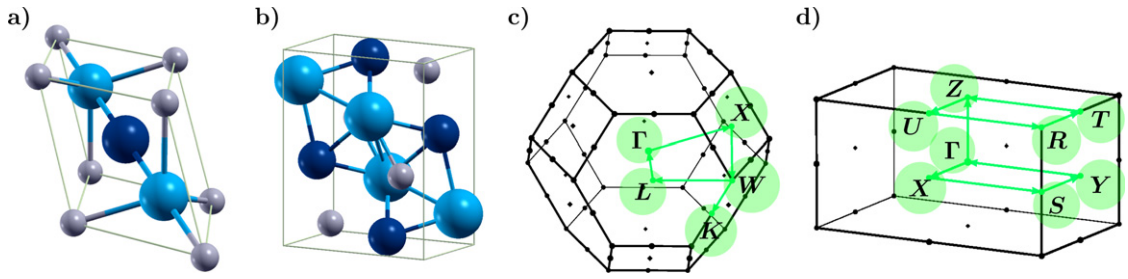

Figure 1. Ball-stick representation of the primitive unit cells of (a) Cs_3Sb and (b) Cs_2Te. Cs atoms in blue (light blue for Cs1 and dark blue for Cs2) and Sb and Te atoms in gray. Brillouin zones of (c) Cs_3Sb and (d) Cs_2Te with high-symmetry points and the path connecting them highlighted. Graphics created with XCrysDen [55].

Table 1. Lattice parameters of the conventional unit cell, volume per atom (Ω), and cohesive energy per atom (E_{coh}) of Cs_3Sb and Cs_2Te.

	PBE	SCAN	HSE06	Exp.
		Cs_3Sb		
a (Å)	9.298	9.194	9.220	9.14–9.19[a]
Ω (Å^3/atom)	50.24	48.58	48.99	47.72–48.51
E_{coh} (eV/atom)	−2.037	−2.436	−2.316	—
		Cs_2Te		
a (Å)	9.542	9.250	9.481	9.109[b]
b (Å)	5.845	5.845	5.811	5.871[b]
c (Å)	11.591	11.598	11.557	11.494[b]
Ω (Å^3/atom)	53.88	52.26	53.06	51.22
E_{coh} (eV/atom)	−2.655	−3.081	−3.037	—

[a] [69, 70, 75, 76].
[b] [80].

self-consistency on the G alleviates the starting-point dependence of the GW_0 calculations, a dependence of the results on the underlying approximation for v_{xc} (PBE, in this case) cannot be entirely ruled out.

3. Results

3.1. Structural properties

We begin our analysis by inspecting the structural properties of both compounds. Two different crystal structures have been reported for Cs_3Sb: a partially ordered NaTl structure [69], and a completely ordered anti-BiF_3 structure [70]. Here, we consider the latter geometry (space group $Fm\bar{3}m$), in line with previous theoretical studies [24, 71–74]. The primitive unit cell consists of three lattice sites for Cs atoms and one lattice site for Sb, see figure 1(a). There are two crystallographically inequivalent lattice sites for Cs, characterized by different coordination and bonding character, which here are denoted as Cs1 and Cs2. The fractional coordinates of Cs1 are $(\frac{1}{4}, \frac{1}{4}, \frac{1}{4})$ and $(\frac{3}{4}, \frac{3}{4}, \frac{3}{4})$ while Cs2 is located at $(\frac{1}{2}, \frac{1}{2}, \frac{1}{2})$. The Sb atom is at the origin, $(0, 0, 0)$.

The experimental lattice parameter of Cs_3Sb, as obtained using x-ray and electron diffraction methods [69, 70, 75, 76], ranges from 9.14 Å to 9.19 Å. In table 1, we compare our DFT results with the above-cited experimental references and, unsurprisingly, we find that PBE overestimates the lattice parameter by 1.18%. This is a well-known problem of this functional and has also been reported for many other bulk materials [45, 77, 78]. Also HSE06 tends to overestimate the lattice parameter, which is understandable considering that the fraction of exact exchange is included on top of a semi-local approximation for v_{xc}. However, this functional leads to a sizable improvement over PBE, yielding lattice vectors only 0.33% larger than the experimental one. The best agreement with experiment is obtained with the SCAN functional, which delivers a value coinciding with the upper boundary of the experimental range (see table 1). The computed unit cell volumes reflect this behavior. A very similar trend in accuracy for the three used functionals has been observed by Zhang *et al* in the analysis of 64 different bulk solid materials [45].

Turning to the cohesive energy, which is calculated by subtracting the total energy of free atoms from the total energy of the crystal unit cell, the SCAN and the HSE06 functionals yield very similar results, with the former featuring a slightly more negative value (see table 1). This finding is consistent with two recent studies

that agree on the superiority of the SCAN functional over PBE in the prediction of accurate formation energies [58, 79]. The PBE functional underestimates the cohesive energy by 0.3–0.4 eV/atom.

Two orthorhombic crystal structures have been identified for Cs_2Te: one with space-group symmetry $P2_12_12_1$ [81], and, more recently, an anti-$PbCl_2$ crystal structure belonging to the space group *Pnma* [80]. Herein, we focus on the latter. The orthorhombic unit cell of Cs_2Te is characterized by the three lattice vectors *a*, *b*, and *c*, and, in addition, by six internal parameters $x_{1,2,3}$ and $z_{1,2,3}$, which are needed to define the atomic positions of the eight cesium and four tellurium atoms. The fractional coordinates of the four lattice sites are $(x_{1,2,3}, \frac{1}{4}, z_{1,2,3})$, $(\frac{1}{2}+x_{1,2,3}, \frac{1}{4}, \frac{1}{2}-z_{1,2,3})$, $(\frac{1}{2}-x_{1,2,3}, \frac{3}{4}, \frac{1}{2}+z_{1,2,3})$ and, $(1-x_{1,2,3}, \frac{2}{4}, 1-z_{1,2,3})$ with the integers 1, 2, 3 representing the positions of Cs1, Cs2, and Te, respectively. The experimental lattice parameters of Cs_2Te, as obtained from x-ray diffraction measurements [80], are reported in table 1. The internal parameters are given in the appendix (table 3).

In the case of Cs_2Te, all the considered functionals overall overestimate the unit cell volume with respect to the measurements. However, the same trend discussed for Cs_3Sb is obtained also for this material: SCAN yields results in closest agreement to the experimental ones, followed by HSE06 and, lastly, by PBE, which gives rise to the largest overestimation. The individual lattice vectors, *a*, *b*, and *c* exhibit a slightly different behavior compared to the whole volume, computed as their product. While the *a* parameter is, like the volume, overestimated by all adopted v_{xc} approximations, with SCAN offering the best performance ($+1.55\%$ compared to the experiment) and PBE the worst one ($+4.75\%$), the *b* vector is *underestimated* by all functionals, with PBE and SCAN giving the same and best result in this case (-0.44% with respect to the experimental reference); the estimate of HSE06 is anyway satisfactory (-1.02% below the experimental target). Finally, for the *c* parameter, HSE06 yields the closest value in comparison with the measurement ($+0.55\%$) while SCAN overestimates the target by $+0.90\%$, performing slightly worse than PBE ($+0.84\%$). As for the cohesive energy, the SCAN and the HSE06 functionals give very similar values, while, once again, the PBE functional predicts the shallowest value, that is about 0.4 eV/atom more positive than the results obtained with the other functionals.

3.2. Electronic properties

After analyzing the structural properties and stability of the considered materials, we now turn to their electronic structure, which is key to understand their behavior as photocathode materials. We start by inspecting the band structure and the DOS, which is further decomposed into atom-projected contributions (see figure 2).

Bulk Cs_3Sb is characterized by an indirect band gap between the high-symmetry points *X* and Γ, in agreement with the predictions of earlier studies [25, 71, 72, 82]. The highest occupied states of Cs_3Sb are dominated by Sb electrons in the 5*p*-shell, giving rise to three low-dispersive bands (see figure 2, left panels). The next valence state is 7.0–7.5 eV deeper in energy compared to the valence-band maximum, and is dominated by Sb *s*-orbitals, as visualized in the projected DOS (PDOS). Occupied Cs states appear at even lower energies, around 9.5–10.0 eV (Cs1) and 10.5–11.5 eV (Cs2), also giving rise to flat 'atomic-like' bands. Identifying the contributions of chemically inequivalent atoms is particularly relevant in view of x-ray spectroscopy studies [25, 74, 83, 84]. In the conduction region of Cs_3Sb, bands are overall much more dispersive (see figure 2, left panels). The bottom of the conduction band at Γ corresponds to the minimum of a parabolic state with Cs1–Cs2 hybridized *sp*-contributions. At higher energies, hybridized *s*- and *d*-states appear.

The general features discussed above, concerning band character and dispersion, are equally reproduced in all our calculations, regardless of the approximation adopted for v_{xc}. The quantity that is mainly affected by the choice of the xc functional is the size of the band gaps (see table 2). In the absence of reliable experimental references (it is very challenging to grow and characterize single crystalline Cs_3Sb samples [85, 86]), we benchmark our DFT results against those obtained with the GW_0 approximation of MBPT. A comparison of the band structure between DFT (PBE functional) and the single-shot G_0W_0 approximation has been reported for Cs_3Sb in reference [25]. As discrepancies concerning band shape and dispersion are found to be marginal, herein, we solely focus on the absolute values of the band gaps.

Given the indirect nature of the electronic gap in Cs_3Sb, which is correctly reproduced by all three considered functionals, it is instructive to inspect also the smallest direct band gap at Γ, hereafter addressed as *optical gap*. Unsurprisingly, the PBE functional underestimates the electronic gap by almost 50% compared to the GW_0 method, in line with previous studies [25, 71, 72, 82]. On the other hand, band-gap values in very good agreement with the benchmark reference are obtained with both SCAN and HSE06: differences with respect to the GW_0 gaps are on the order of 15 meV.

Similar trends are obtained also for the optical gaps, however, with some remarkable differences (see table 2). The PBE result is only about 3 5% below the GW_0 one, in agreement with previous studies [25, 71, 72], while both SCAN and HSE06 values depart from the reference by about 100 meV. The reason for the different

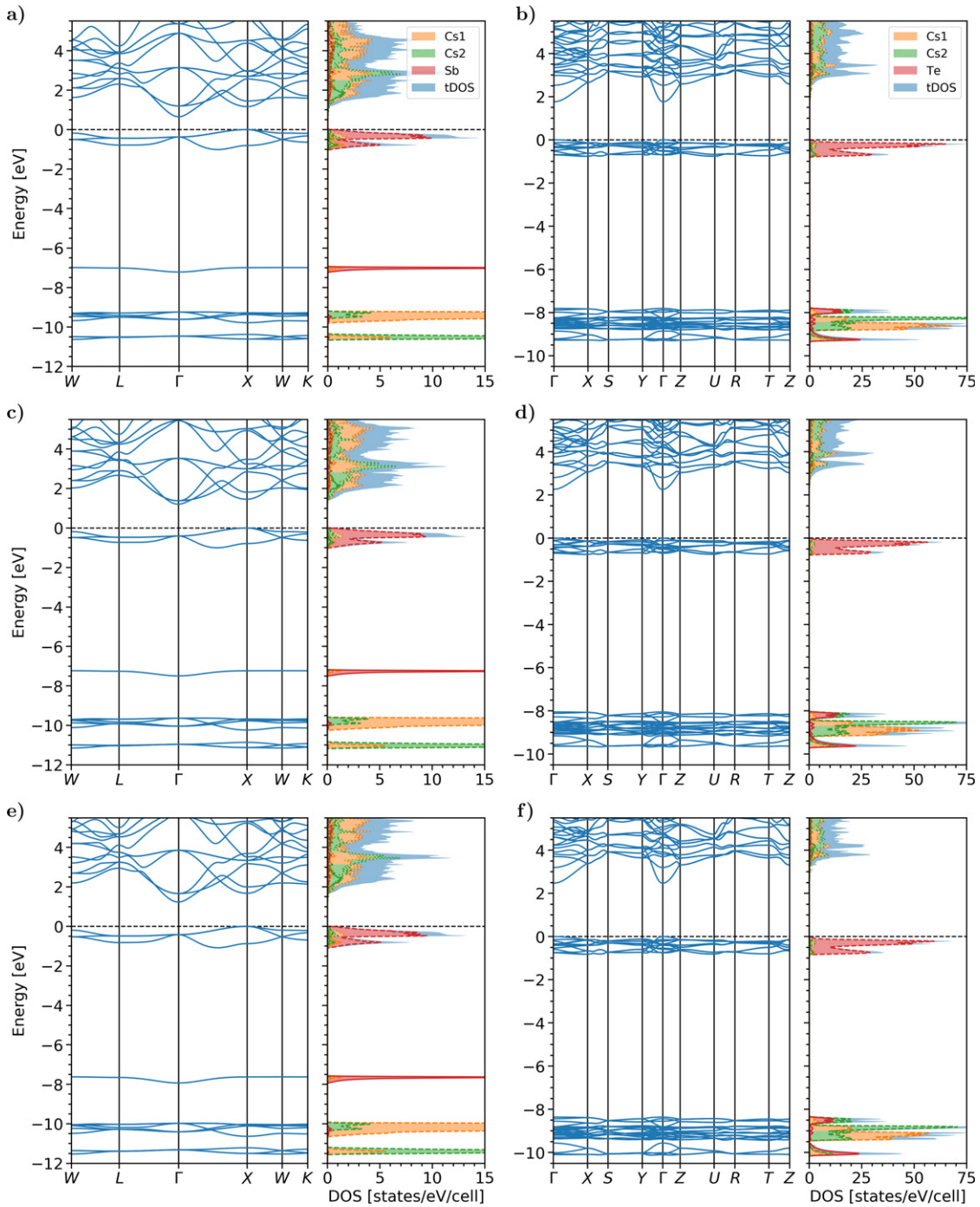

Figure 2. Band structure and PDOS of Cs_3Sb (left) and Cs_2Te (right) obtained with PBE (panels (a) and (b)), SCAN ((c) and (d)), and HSE06 functional ((e) and (f)). The energy is set to zero at the valence band maximum (dashed line). Solid, dashed, dotted and dash-dotted lines represent contributions from *s*-, *p*-, *d*- and *f*-orbitals, respectively.

behavior of optical and electronic gaps can be understood through a close inspection of the band structures (see figure 2, left panels). In the conduction region, the relative energy separation between the lowest-lying bands is critically sensitive to the xc functional. While PBE features a separation of about 0.54 eV between the conduction band minimum and the next bands around Γ [see figure 2(a)], this value is drastically reduced in the band structures obtained with SCAN [0.17 eV, see figure 2(c)] and also with HSE06 [figure 2(e)], even though to a slightly lesser extent (0.43 eV). This variation results in an overall reduction in the energy difference between the conduction band minimum at Γ and the subsequent minimum at *X* of 267 meV for SCAN and 74 meV for HSE06. At higher energies the unoccupied states are reproduced analogously by all three functionals, although absolute energies are generally lower in the PBE result compared to the other two. We see a similar trend also in the valence bands: the energy separation between highest-occupied bands and the next (flat) one depends on the adopted xc functional (see figure 2, left panels). In the PBE band structure, this band appears

Table 2. Electronic and optical gaps including SOC of Cs_3Sb and Cs_2Te in eV.

	PBE	SCAN	HSE06	GW_0	Exp.
			Cs_3Sb		
E_{gap}	0.65	1.21	1.24	1.22	
E_{gap}^{opt}	1.03	1.46	1.65	1.56	
E_{gap} + SOC	0.51	1.06	1.10	—	1.60[a]
E_{gap}^{opt} + SOC	0.85	1.31	1.48	—	
			Cs_2Te		
E_{gap}	1.76	2.26	2.47	2.63	
E_{gap}^{opt}	1.76	2.26	2.47	2.63	
E_{gap} + SOC	1.58	2.06	2.30	—	3.3[b]
E_{gap}^{opt} + SOC	1.58	2.06	2.30	—	

[a] [87].
[b] [88].

at approximately 7.0 eV, while its energy decreases in the SCAN (7.2 eV) and HSE06 result (7.6 eV). The same trend is followed qualitatively and quantitatively also by the deepest manifold of occupied bands displayed in figure 2, left panels.

Cs_2Te has a direct band gap at the Γ-point (see figure 2, right panels): hence, in this material, electronic and optical gaps coincide. Similar to Cs_3Sb, also in Cs_2Te the uppermost occupied bands bear mainly *p*-character of the anion, which is here the Te atoms. However, in this case, a manifold of 12 bands is found at the top of the valence region since the unit cell contains 4 Te atoms. Also, in analogy with Cs_3Sb, the next occupied states are largely separated in energy from the latter (7.8–8.4 eV below the valence band maximum). In this region, bands are highly hybridized despite their low dispersion, exhibiting contributions from both Te *s*- and Cs *p*-states. The conduction bands of Cs_2Te are slightly more dispersive than the valence ones, especially in the vicinity of the minimum at Γ, where the lowest-unoccupied band exhibits a parabolic-like shape, as a fingerprint of the *s*-orbitals of both species dominating that state. Energetically higher conduction bands show low dispersion and the signatures of hybridization between *d*- and *s*-states of Cs and Te.

The above-mentioned features are qualitatively captured by all three considered functionals, as in the case of Cs_3Sb. Again and expectedly, PBE leads to an underestimation of the gap by about one third in comparison to our GW_0 result (see table 2). Our PBE result is in good agreement with the value reported in reference [89]. Also SCAN and HSE06 give rise to smaller band-gaps compared to the GW_0 reference by 350 meV and 150 meV, respectively.

Differences in the relative band energies induced by different approximations of v_{xc} are less pronounced in Cs_2Te compared to Cs_3Sb (see figure 2, right panels). The separation between the conduction band minimum and the next unoccupied band at Γ varies only by 40 meV between PBE and HSE06 and, again, to a larger amount for SCAN (210 meV). The width of the highest-energy valence band manifold is equally captured by all xc functionals. Deeper bands are found starting from −7.8 eV (PBE), −8.0 eV (SCAN), and −8.4 eV (HSE06) with respect to the valence-band top set to zero in figure 2, right panels.

The comparison of the computed band gaps with the experimental ones is a delicate matter. Reference values are available for Cs_3Sb [87] and Cs_2Te [88], which both correspond to rather old measurements. Given the well-known experimental difficulties in controlling the composition and the quality of the samples of both materials [86, 90], it is wise to handle these data with care in a comparison with *ab initio* results obtained for stoichiometric materials in ideal bulk unit cells. Under these premises, we notice that the experimental gap available for Cs_3Sb, obtained from photoconductivity and photoabsorption measurements [87], matches well with the optical band gap calculated with HSE06. On the other hand, the experimental gap of Cs_2Te (3.3 eV resulting from photoemission spectroscopy [88]) overestimates all calculated data, including the one from GW_0, by at least 0.5 eV. Systematic first-principles studies and new measurements are needed for a final assessment of this point.

3.3. The impact of SOC

SOC is a relativistic effect that can have a non-negligible impact on the electronic structure of materials formed by heavy atoms. In order to assess the role of SOC in the two investigated systems, Cs_3Sb and Cs_2Te, and the capability of the considered approximations for v_{xc} to capture it, we performed an additional set of calculations, the result of which we contrast with those discussed above. In this analysis, we focus on a window of approximately 5 eV around the gap region. At a first glance, it is clear that in both materials SOC affects the occupied bands much stronger than the unoccupied ones (see figure 3). In Cs_3Sb, the valence bands exhibit

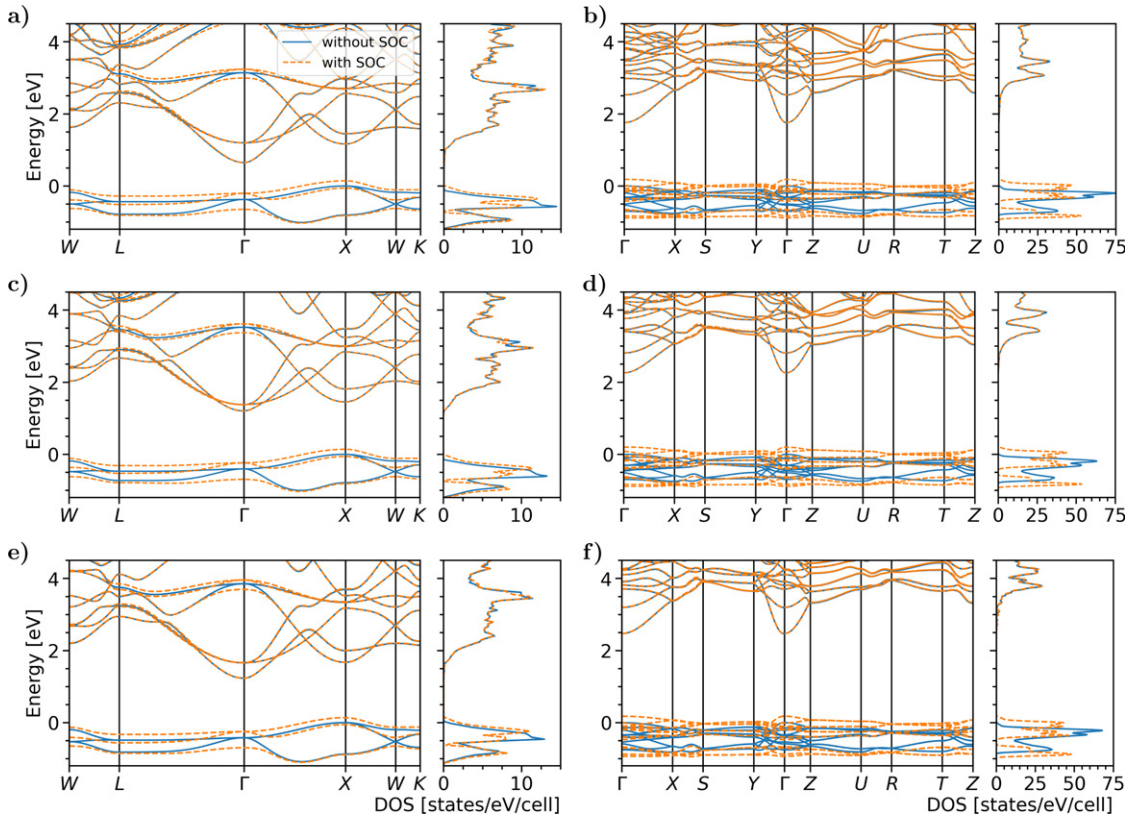

Figure 3. Band structures and DOS close to the gap region of Cs_3Sb (left) and Cs_2Te (right), computed from DFT using (a)–(b) PBE, (c)–(d) SCAN, and (e)–(f) HSE06 functional with and without SOC, solid and dashed lines, respectively. The valence band maxima without SOC correction is set to zero in all plots.

an SOC-induced splitting of about 0.25 eV and 0.45 eV at the high symmetry points W and Γ, respectively. Additionally, the uppermost occupied band is slightly shifted upwards under the effect of SOC. Considering that the conduction-band minimum is unaltered by SOC, the band gap is overall decreased by approximately 0.15 eV, see table 2. A similar effect is noted also in the conduction region, again close to Γ, where the two degenerate bands at approximately 3 eV in figure 3(a) are split by 0.24 eV under the effect of SOC. This feature is so localized in **k**-space that it is hardly appreciable in the plot of the DOS.

In Cs_2Te, the changes in the band structure induced by SOC are more pronounced than in Cs_3Sb. The valence bands are pulled apart such that the upper states are up-shifted and the lower ones are down-shifted compared to their counterparts computed without SOC (see figure 3, right panels), resulting in an overall splitting of 0.2 eV. As an additional effect, SOC reduces the band dispersion, especially along the path between the high symmetry points S and Y as well as between Z and U, where the states are almost flat. The conduction region of Cs_2Te is totally unaffected by SOC: both band structures and DOS displayed in figure 3, right panels, overlap with the results obtained without SOC.

No remarkable difference related to SOC splittings are appreciated among the results obtained with different approximations for v_{xc} in both materials. Differences in the calculated band-gaps are in line with those obtained neglecting SOC (see table 2). Our PBE and HSE06 results for Cs_3Sb follow qualitatively the same trend shown in reference [82]. This is to be expected, as SOC is a physical effect that does not depend on the details of the approximations adopted for v_{xc}. This finding has an important implication: if one is interested solely in the SOC splittings, a semi-local functional will be sufficient to capture them.

4. Summary and conclusions

We studied the performance of different levels of approximations for the exchange–correlation potential (PBE, SCAN, and HSE06) in DFT calculations on cesium antimonide and cesium telluride, both being actively used as photocathode materials for vacuum electron sources. We focused on the structural and electronic properties of these two bulk crystals, including the effects of SOC. We found that all adopted approximations tend to

overestimate the unit cell volume of both materials in comparison to the experimental references, with the PBE functional showing the largest discrepancies and the SCAN functional reproducing most accurately the experimental lattice parameters. All explored functionals predict the same qualitative features in the electronic structures of the materials, including band-gap character, band dispersion, and atom-projected contributions to the total DOS. Differences among the adopted approximations arise in terms of band energies, including the values of the electronic and optical gaps. As expected, the PBE functional largely underestimates these quantities in both materials, while both SCAN and HSE06 yield values in much better agreement with the GW_0 reference, adopted in absence of reliable experimental data. The gaps resulting from the HSE06 approximation are the closest to the GW_0 benchmark, followed by those delivered by SCAN, which are systematically lower by about 0.2 eV.

In both materials, SOC induces band splittings in the valence region; in Cs_3Sb, additional splittings appear also in the conduction region. In Cs_3Sb, the band splittings occur in the vicinity of the high-symmetry points Γ and W, while in Cs_2Te the internal splitting in the valence region its the width of this band by approximately 0.2 eV. As a result of SOC, the band gap of both materials is decreased by a corresponding amount of energy. These effects are reproduced almost identically by all considered functionals: approximations in the treatment of relativistic effects impact the description of this property much more strongly than the one on v_{xc}.

In conclusion, our results indicate SCAN as the optimal choice to approximate the exchange–correlation potential in DFT calculations of Cs-based antimonide and telluride materials. Both structural and electronic properties are reliably reproduced at computational costs that are only slightly larger than those of generalized gradient approximations of v_{xc} (see table 4 in the appendix). In agreement with the current knowledge, we found that PBE is suitable for simulating structural parameters but should be avoided in the quantitative description of the electronic properties. Compared to the popular range-separated hybrid functional HSE06, in the considered materials, SCAN produces superior outcomes in terms of lattice vectors and unit-cell volumes. On the other hand, HSE06 results for electronic and optical gaps are systematically closer to the GW_0 reference. This is not surprising, as this hybrid functional has been specifically developed to accurately reproduce band gaps by means of DFT. The computational costs demanded by HSE06 are, however, generally higher compared to SCAN, which makes the latter a more convenient choice in the study of surfaces and defected bulks requiring large supercells. The ability of SCAN to reproduce the electronic properties of the considered Cs-based materials can be ascribed to the orbital character of the bands in the vicnity of the gap. As shown in figure 2, the valence and conduction regions of both Cs_3Sb and Cs_2Te are dominated by *s*- and *p*-orbitals, for which already the GGA approximation works fairly well. This finding and the proposed rationale suggests that any meta-GGA implementation may work well for these classes of systems. However, the numerical performance can critically depend on the details of the specific parameterization and should be therefore carefully assessed.

The all-electron implementation adopted in this study makes our findings independent of the description of core levels via different pseudopotential recipes. The use of this approximation requires, therefore, dedicated benchmark studies. Likewise, the choice of the basis set (e.g. plane waves) introduces additional parameters, such as the plane-wave cutoff, that have to be carefully evaluated for convergence. Our work represents therefore a cornerstone for the systematic assessment of various approximations and parameters in the DFT simulations of crystalline Cs-based photocathode compounds, and their impact in describing relevant properties. This is vital for predictive high-throughput screening on such systems, which can greatly contribute to the discovery and development of novel and more efficient materials for vacuum electron sources.

Acknowledgments

We are grateful for Jannis Krumland and Raymond Amador for their suggestions on the unpublished manuscript. This work is funded by the German Federal Ministry of Education and Research (Professorinnenprogramm III) as well as from the Lower Saxony State (Professorinnen für Niedersachsen). Computational resources provided by the North-German Supercomputing Alliance (HLRN), Project bep00084, and by the HPC cluster CARL at the University of Oldenburg, funded by the DFG (Project No. INST 184/157-1 FUGG) and by the Ministry of Science and Culture of the Lower Saxony State.

Data availability statement

The data that support the findings of this study are available upon reasonable request from the authors.

Table 3. Internal lattice parameters for Cs_2Te computed from DFT with different approximations for v_{xc} and compared with the available experimental reference [80].

	PBE	SCAN	HSE06	Exp. [80]
x_1	0.028	0.035	0.029	0.016
z_1	0.172	0.183	0.173	0.180
x_2	0.146	0.154	0.147	0.152
z_2	0.572	0.571	0.572	0.568
x_3	0.246	0.241	0.246	0.248
z_3	0.886	0.886	0.885	0.888

Table 4. Comparison among PBE, SCAN, and rSCAN functionals in terms of the average run time needed per self-consistent iteration (t_{av}), and the number of iterations needed to converge the solution of the KS equations.

	Cs_3Sb			Cs_2Te		
	PBE	SCAN	rSCAN	PBE	SCAN	rSCAN
t_{av} (s)	4.43	5.49	5.36	7.71	10.31	10.07
Nr. of iterations	17	24	21	16	23	18

Table 5. Lattice parameters of the conventional unit cell, volume per atom (Ω), and cohesive energy per atom (E_{coh}) of Cs_3Sb and Cs_2Te comparing the SCAN and the rSCAN functional.

	a (Å)		Ω (Å^3/atom)		E_{coh} (eV/atom)
			Cs_3Sb		
SCAN	9.194		48.58		−2.436
rSCAN	9.238		49.27		−2.371
	a (Å)	b (Å)	c (Å)	Ω (Å^3/atom)	E_{coh} (eV/atom)
			Cs_2Te		
SCAN	9.250	5.845	11.598	52.26	−3.081
rSCAN	9.456	5.849	11.611	53.52	−3.016

Table 6. Electronic and optical gaps including SOC of Cs_3Sb and Cs_2Te in eV comparing the SCAN and rSCAN functional.

	E_{gap}	E_{gap}^{opt}	E_{gap} + SOC	E_{gap}^{opt} + SOC
		Cs_3Sb		
SCAN	1.21	1.46	1.06	1.31
rSCAN	1.15	1.44	1.01	1.30
		Cs_2Te		
SCAN	2.26	2.26	2.06	2.06
rSCAN	2.19	2.19	2.00	2.00

Appendix.

In table 3, we report the calculated internal lattice parameters of Cs_2Te. In table 4,we compare the performance of PBE, SCAN, and rSCAN for calculations run on the same computational infrastructure. It can be seen that both the average run time per self-consistent iteration (t_{av}) and the number of iterations needed for convergence are comparable. The rSCAN functional shows a slightly improved performance compared to the original SCAN functional.

Tables 5 and 6, as well as figure 4 present the comparison between the performances of SCAN [49] and rSCAN [30] functionals. We notice slightly increased unit cell volumes and slightly more positive values of the cohesive energy given by the rSCAN functional in comparison with SCAN (table 5). Differences in the band gaps are smaller than 0.1 eV, with the rSCAN functional yielding lower values (table 6). However, no visible differences are found in the band structures computed with the two functionals (see figure 4).

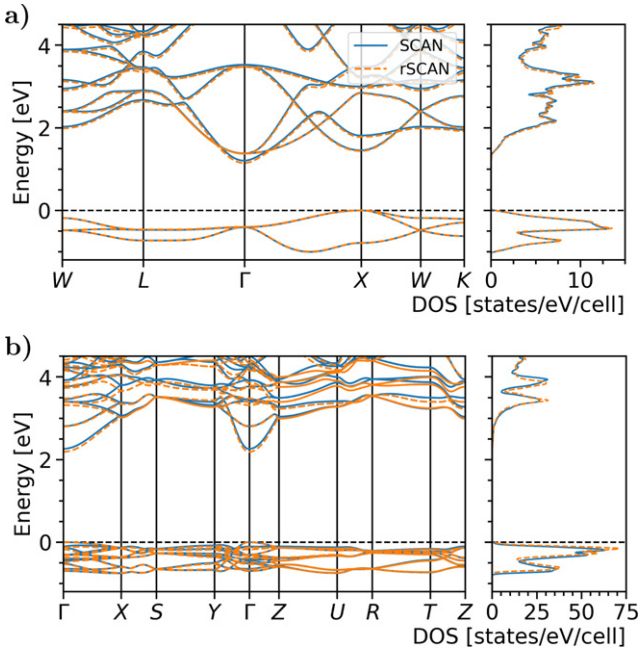

Figure 4. Band structure and total DOS of Cs_3Sb (top) and Cs_2Te (bottom) for the SCAN and rSCAN functional.

ORCID iDs

Holger-Dietrich Saßnick https://orcid.org/0000-0001-8887-9248
Caterina Cocchi https://orcid.org/0000-0002-9243-9461

References

[1] Hernandez-Garcia C, O'Shea P G and Stutzman M L 2008 Electron sources for accelerators *Phys. Today* **61** 44
[2] Dowell D H *et al* 2010 Cathode R & D for future light sources *Nucl. Instrum. Methods Phys. Res.* A **622** 685
[3] Xiang R and Teichert J 2015 Photocathodes for high brightness photo injectors *Phys. Procedia* **77** 58
[4] Smedley J, Rao T and Wang E 2009 K_2CsSb cathode development *AIP Conf. Proc.* **1149** 1062
[5] Vecchione T, Ben-Zvi I, Dowell D H, Feng J, Rao T, Smedley J, Wan W and Padmore H A 2011 A low emittance and high efficiency visible light photocathode for high brightness accelerator-based x-ray light sources *Appl. Phys. Lett.* **99** 034103
[6] Dolizy P, Grolière F and Lemonier M 1988 High performance with trialkaline antimonide photocathodes *Advances in Electronics and Electron Physics* vol 74 (Amsterdam: Elsevier) pp 331–8
[7] Musumeci P, Giner Navarro J, Rosenzweig J B, Cultrera L, Bazarov I, Maxson J, Karkare S and Padmore H 2018 Advances in bright electron sources *Nucl. Instrum. Methods Phys. Res.* A **907** 209
[8] Karkare S, Boulet L, Cultrera L, Dunham B, Liu X, Schaff W and Bazarov I 2014 Ultrabright and ultrafast III–V semiconductor photocathodes *Phys. Rev. Lett.* **112** 097601
[9] Orlov D A, Weigel U, Schwalm D, Terekhov A S and Wolf A 2004 Ultra-cold electron source with a GaAs-photocathode *Nucl. Instrum. Methods Phys. Res.* A **532** 418
[10] Xu Y, Zhang Y, Feng C, Shi F, Zou J, Chen X and Chang B 2016 Differences in stability and repeatability between GaAs and GaAlAs photocathodes *Opt. Commun.* **380** 320
[11] Pong W 1972 Scattering effects in photoelectric emission from PbTe films *J. Appl. Phys.* **43** 60
[12] Li T and Schroeder W A 2017 PbTe (111) sub-thermionic photocathode: a route to high-quality electron pulses (arXiv:1704.00194)
[13] Di Bona A, Sabary F, Joly S, Michelato P, Sertore D, Pagani C and Valeri S 1997 Development, operation and analysis of bialkali antimonide photocathodes for high-brightness photo-injectors *Nucl. Instrum. Methods Phys. Res.* A **385** 385
[14] Bazarov I, Cultrera L, Bartnik A, Dunham B, Karkare S, Li Y, Liu X, Maxson J and Roussel W 2011 Thermal emittance measurements of a cesium potassium antimonide photocathode *Appl. Phys. Lett.* **98** 224101
[15] Feng J, Karkare S, Nasiatka J, Schubert S, Smedley J and Padmore H 2017 Near atomically smooth alkali antimonide photocathode thin films *J. Appl. Phys.* **121** 044904
[16] Ding Z, Gaowei M, Sinsheimer J, Xie J, Schubert S, Padmore H, Muller E and Smedley J 2017 *In situ* synchrotron x-ray characterization of K_2CsSb photocathode grown by ternary co-evaporation *J. Appl. Phys.* **121** 055305
[17] Xie J *et al* 2017 Synchrotron x-ray study of a low roughness and high efficiency K_2CsSb photocathode during film growth *J. Phys. D: Appl. Phys.* **50** 205303
[18] Schmeißer M A, Mistry S, Kirschner H, Schubert S, Jankowiak A, Kamps T and Kühn J 2018 Towards the operation of Cs-K-Sb photocathodes in superconducting rf photoinjectors *Phys. Rev. Accel. Beams* **21** 113401
[19] Draxl C and Scheffler M 2018 Nomad: the fair concept for big data-driven materials science *MRS Bull.* **43** 676
[20] Jain A *et al* 2013 Commentary: the materials project: a materials genome approach to accelerating materials innovation *APL Mater.* **1** 011002
[21] Saal J E, Kirklin S, Aykol M, Meredig B and Wolverton C 2013 Materials design and discovery with high-throughput density functional theory: the open quantum materials database (OQMD) *J. Miner. Met. Mater. Soc.* **65** 1501

[22] Talirz L *et al* 2020 Materials cloud, a platform for open computational science *Sci. Data* **7** 299
[23] Antoniuk E R, Yue Y, Zhou Y, Schindler P, Schroeder W A, Dunham B, Pianetta P, Vecchione T and Reed E J 2020 Generalizable density functional theory based photoemission model for the accelerated development of photocathodes and other photoemissive devices *Phys. Rev.* B **101** 235447
[24] Cocchi C, Mistry S, Schmeißer M, Kühn J and Kamps T 2018 First-principles many-body study of the electronic and optical properties of CsK_2Sb, a semiconducting material for ultra-bright electron sources *J. Phys. Condens. Matter.* **31** 014002
[25] Cocchi C, Mistry S, Schmeißer M, Amador R, Kühn J and Kamps T 2019 Electronic structure and core electron fingerprints of caesium-based multi-alkali antimonides for ultra-bright electron sources *Sci. Rep.* **9** 18276
[26] Burke K 2012 Perspective on density functional theory *J. Chem. Phys.* **136** 150901
[27] Mardirossian N and Head-Gordon M 2017 Thirty years of density functional theory in computational chemistry: an overview and extensive assessment of 200 density functionals *Mol. Phys.* **115** 2315
[28] Tao J and Mo Y 2016 Accurate semilocal density functional for condensed-matter physics and quantum chemistry *Phys. Rev. Lett.* **117** 073001
[29] Patra B, Jana S, Constantin L A and Samal P 2019 Relevance of the Pauli kinetic energy density for semilocal functionals *Phys. Rev.* B **100** 155140
[30] Bartók A P and Yates J R 2019 Regularized scan functional *J. Chem. Phys.* **150** 161101
[31] Furness J W, Kaplan A D, Ning J, Perdew J P and Sun J 2020 Accurate and numerically efficient r^2SCAN meta-generalized gradient approximation *J. Phys. Chem. Lett.* **11** 8208
[32] Zhou Y, Wu J, Chen S and Chen G 2019 Toward the exact exchange–correlation potential: a three-dimensional convolutional neural network construct *J. Phys. Chem. Lett.* **10** 7264
[33] Dick S and Fernandez-Serra M 2020 Machine learning accurate exchange and correlation functionals of the electronic density *Nat. Commun.* **11** 3509
[34] Peng H, Yang Z-H, Perdew J P and Sun J 2016 Versatile van der Waals density functional based on a meta-generalized gradient approximation *Phys. Rev.* X **6** 041005
[35] Caldeweyher E, Ehlert S, Hansen A, Neugebauer H, Spicher S, Bannwarth C and Grimme S 2019 A generally applicable atomic-charge dependent London dispersion correction *J. Chem. Phys.* **150** 154122
[36] Chakraborty D, Berland K and Thonhauser T 2020 Next-generation nonlocal van der Waals density functional *J. Chem. Theory Comput.* **16** 5893
[37] Hermann J and Tkatchenko A 2020 Density functional model for van der Waals interactions: unifying many-body atomic approaches with nonlocal functionals *Phys. Rev. Lett.* **124** 146401
[38] Levchenko S V, Ren X, Wieferink J, Johanni R, Rinke P, Blum V and Scheffler M 2015 Hybrid functionals for large periodic systems in an all-electron, numeric atom-centered basis framework *Comput. Phys. Commun.* **192** 60
[39] Barnes T A, Kurth T, Carrier P, Wichmann N, Prendergast D, Kent P R C and Deslippe J 2017 Improved treatment of exact exchange in quantum espresso *Comput. Phys. Commun.* **214** 52
[40] Lehtola S, Steigemann C, Oliveira M J T and Marques M A L 2018 Recent developments in LIBXC—a comprehensive library of functionals for density functional theory *SoftwareX* **7** 1
[41] Skelton J M, Parker S C, Togo A, Tanaka I and Walsh A 2014 Thermal physics of the lead chalcogenides PbS, PbSe, and PbTe from first principles *Phys. Rev.* B **89** 205203
[42] Mo Y, Car R, Staroverov V N, Scuseria G E and Tao J 2017 Assessment of the Tao-Mo nonempirical semilocal density functional in applications to solids and surfaces *Phys. Rev.* B **95** 035118
[43] Jana S, Sharma K and Samal P 2018 Assessing the performance of the recent meta-GGA density functionals for describing the lattice constants, bulk moduli, and cohesive energies of alkali, alkaline-earth, and transition metals *J. Chem. Phys.* **149** 164703
[44] Jana S, Patra A and Samal P 2018 Assessing the performance of the Tao-Mo semilocal density functional in the projector-augmented-wave method *J. Chem. Phys.* **149** 044120
[45] Zhang G-X, Reilly A M, Tkatchenko A and Scheffler M 2018 Performance of various density-functional approximations for cohesive properties of 64 bulk solids *New J. Phys.* **20** 063020
[46] Borlido P, Aull T, Huran A W, Tran F, Marques M A L and Botti S 2019 Large-scale benchmark of exchange–correlation functionals for the determination of electronic band gaps of solids *J. Chem. Theory Comput.* **15** 5069
[47] Tran F, Doumont J, Kalantari L, Huran A W, Marques M A L and Blaha P 2019 Semilocal exchange–correlation potentials for solid-state calculations: current status and future directions *J. Appl. Phys.* **126** 110902
[48] Perdew J P, Burke K and Ernzerhof M 1996 Generalized gradient approximation made simple *Phys. Rev. Lett.* **77** 3865
[49] Sun J, Ruzsinszky A and Perdew J P 2015 Strongly constrained and appropriately normed semilocal density functional *Phys. Rev. Lett.* **115** 036402
[50] Heyd J, Scuseria G E and Ernzerhof M 2003 Hybrid functionals based on a screened coulomb potential *J. Chem. Phys.* **118** 8207
[51] Verma P and Truhlar D G 2017 HLE17: an improved local exchange–correlation functional for computing semiconductor band gaps and molecular excitation energies *J. Phys. Chem* C **121** 7144
[52] Mejia-Rodriguez D and Trickey S 2018 Deorbitalized meta-GGA exchange–correlation functionals in solids *Phys. Rev.* B **98** 115161
[53] Aschebrock T and Kümmel S 2019 Ultranonlocality and accurate band gaps from a meta-generalized gradient approximation *Phys. Rev. Res.* **1** 033082
[54] Borlido P, Schmidt J, Huran A W, Tran F, Marques M A and Botti S 2020 Exchange–correlation functionals for band gaps of solids: benchmark, reparametrization and machine learning *npj Comput. Mater.* **6** 1
[55] Kokalj A 1999 XCrySDen—a new program for displaying crystalline structures and electron densities *J. Mol. Graph. Model.* **17** 176
[56] Hohenberg P and Kohn W 1964 Inhomogeneous electron gas *Phys. Rev.* **136** B864
[57] Kohn W and Sham L J 1965 Self-consistent equations including exchange and correlation effects *Phys. Rev.* **140** A1133
[58] Zhang Y *et al* 2018 Efficient first-principles prediction of solid stability: towards chemical accuracy *npj Comput. Mater.* **4** 9
[59] Chen M *et al* 2017 *Ab initio* theory and modeling of water *Proc. Natl Acad. Sci. USA* **114** 10846
[60] Csonka G I, Perdew J P and Ruzsinszky A 2010 Global hybrid functionals: a look at the engine under the hood *J. Chem. Theory Comput.* **6** 3688
[61] Henderson T M, Paier J and Scuseria G E 2011 Accurate treatment of solids with the HSE screened hybrid *Phys. Status Solidi b* **248** 767
[62] Blum V, Gehrke R, Hanke F, Havu P, Havu V, Ren X, Reuter K and Scheffler M 2009 *Ab initio* molecular simulations with numeric atom-centered orbitals *Comput. Phys. Commun.* **180** 2175

[63] Huhn W P and Blum V 2017 One-hundred-three compound band-structure benchmark of post-self-consistent spin–orbit coupling treatments in density functional theory *Phys. Rev. Mater.* **1** 033803

[64] Hedin L 1965 New method for calculating the one-particle Green's function with application to the electron-gas problem *Phys. Rev.* **139** A796

[65] von Barth U and Holm B 1996 Self-consistent GW_0 results for the electron gas: fixed screened potential W_0 within the random-phase approximation *Phys. Rev.* B **54** 8411

[66] Shishkin M and Kresse G 2007 Self-consistent *GW* calculations for semiconductors and insulators *Phys. Rev.* B **75** 235102

[67] Gulans A, Kontur S, Meisenbichler C, Nabok D, Pavone P, Rigamonti S, Sagmeister S, Werner U and Draxl C 2014 exciting: a full-potential all-electron package implementing density-functional theory and many-body perturbation theory *J. Phys.: Condens. Matter.* **26** 363202

[68] Nabok D, Gulans A and Draxl C 2016 Accurate all-electron G_0W_0 quasiparticle energies employing the full-potential augmented plane-wave method *Phys. Rev.* B **94** 035118

[69] Jack K H, Wachtel M M and Bragg W L 1957 The characterization and crystal structure of caesium antimonide, a photo-electric surface material *Proc. R. Soc.* A **239** 46

[70] Gnutzmann G, Wilhelm Dorn F and Klemm W 1961 Das Verhalten der Alkalimetalle zu Halbmetallen. VII. Über einige A_3B- und AB_2-Verbindungen der schweren Alkalimetalle mit Elementen der V. Gruppe *Z. Anorg. Allg. Chem.* **309** 210

[71] Wei S-H and Zunger A 1987 Electronic structure of M_3ISb-type filled tetrahedral semiconductors *Phys. Rev.* B **35** 3952

[72] Kalarasse L, Bennecer B and Kalarasse F 2010 Optical properties of the alkali antimonide semiconductors Cs_3Sb, Cs_2KSb, CsK_2Sb and K_3Sb *J. Phys. Chem. Solids* **71** 314

[73] Kalarasse L, Bennecer B, Kalarasse F and Djeroud S 2010 Pressure effect on the electronic and optical properties of the alkali antimonide semiconductors Cs_3Sb, KCs_2Sb, CsK_2Sb and K_3Sb: ab initio study *J. Phys. Chem. Solids* **71** 1732

[74] Cocchi C 2020 X-ray absorption fingerprints from Cs atoms in Cs_3Sb *Phys. Status Solidi RRL* **14** 2000194

[75] Robbie J C and Beck A H 1973 Scanning electron diffraction studies on caesium antimonide photocathodes during formation *J. Phys. D: Appl. Phys.* **6** 1381

[76] Barois J M, Fouassier C, Onillon M and Tanguy B 1989 Experimental study of the non stoichiometry of cesium antimonide $\approx$ Cs_3Sb *Mater. Chem. Phys.* **24** 189

[77] Schimka L, Harl J and Kresse G 2011 Improved hybrid functional for solids: the HSEsol functional *J. Chem. Phys.* **134** 024116

[78] Tran F, Stelzl J and Blaha P 2016 Rungs 1 to 4 of DFT Jacob's ladder: extensive test on the lattice constant, bulk modulus, and cohesive energy of solids *J. Chem. Phys.* **144** 204120

[79] Yang J H, Kitchaev D A and Ceder G 2019 Rationalizing accurate structure prediction in the meta-GGA scan functional *Phys. Rev.* B **100** 035132

[80] Schewe-Miller I and Böttcher P 1991 Synthesis and crystal structures of K_5Se_3, Cs_5Te_3 and Cs_2Te *Z. Kristallogr.* **196** 137

[81] Prins G and Cordfunke E H P 1984 Compounds in the system Cs-Te at room temperature *J. Less Common Met.* **104** L1

[82] Guo S-D 2014 Electronic structures and elastic properties of X_3Sb (x = Li, K, Cs) from the first-principles calculations *Mater. Res. Express* **1** 015906

[83] Cocchi C, Zschiesche H, Nabok D, Mogilatenko A, Albrecht M, Galazka Z, Kirmse H, Draxl C and Koch C T 2016 Atomic signatures of local environment from core-level spectroscopy in β–Ga_2O_3 *Phys. Rev.* B **94** 075147

[84] Vorwerk C, Cocchi C and Draxl C 2017 Addressing electron–hole correlation in core excitations of solids: an all-electron many-body approach from first principles *Phys. Rev.* B **95** 155121

[85] Cultrera L, Lee H and Bazarov I 2016 Alkali antimonides photocathodes growth using pure metals evaporation from effusion cells *J. Vac. Sci. Technol.* B **34** 011202

[86] Galdi A, DeBenedetti W J I, Balajka J, Cultrera L, Bazarov I V, Maxson J M and Hines M A 2020 The effects of oxygen-induced phase segregation on the interfacial electronic structure and quantum efficiency of Cs_3Sb photocathodes *J. Chem. Phys.* **153** 144705

[87] Spicer W E 1958 Photoemissive, photoconductive, and optical absorption studies of alkali-antimony compounds *Phys. Rev.* **112** 114

[88] Powell R A, Spicer W E, Fisher G B and Gregory P 1973 Photoemission studies of cesium telluride *Phys. Rev.* B **8** 3987

[89] Terdik J Z, Németh K, Harkay K C, Terry J H, Spentzouris L, Velázquez D, Rosenberg R and Srajer G 2012 Anomalous work function anisotropy in ternary acetylides *Phys. Rev.* B **86** 035142

[90] Prat E, Bettoni S, Braun H-H, Ganter R and Schietinger T 2015 Measurements of copper and cesium telluride cathodes in a radio-frequency photoinjector *Phys. Rev. Accel. Beams* **18** 043401